Contents lists available at ScienceDirect

Arabian Journal of Chemistry

journal homepage: www.ksu.edu.sa

Original article

The preparation of LaOCl doped carbon-based catalysts and their oxygen reduction reaction performance

Penghua Chen, Jingchun Jia *, Zhe Cheng, Ying Chang, Shaohong Guo, Meilin Jia *

College of Chemistry and Environmental Science, Inner Mongolia Key Laboratory of Green Catalysis and Inner Mongolia Collaborative Innovation Center for Water Environment Safety, Inner Mongolia Normal University, Hohhot 010022, China

ARTICLE INFO

Keywords:
Oxygen reduction reactions
Electrochemical oxidation
Organic pollutants
Rare earth elements

ABSTRACT

Oxygen reduction reaction is a key reaction in fuel cells, and it is crucial to seek catalysts with better oxygen reduction performance. Rare earth metals are applied to the oxygen reduction reaction because of their special electronic structure. La in rare earth elements is an F-region element, which has a typical 4f electron configuration, and can transfer 4f electrons between f-f configuration and f-d configuration to form a unique bond, which can show good electrochemical properties. Based on the regional characteristics of Inner Mongolia, in this paper, a rare earth composite biomass carbon based catalyst was synthesized by high temperature calcination and other operations using milk as a biomass based carbon source and NaCl as a template agent. The catalyst was optimized and it was determined that the H_2O_2 yield of LaOCl-NPC catalyst reached 70 % at a milk to NaCl ratio of 1:10, metal mass ratio of 6 % and calcination temperature of 1200 °C, and showed some ability to treat pollutants in water after the addition of organic pollutants.

1. Introduction

Oxygen reduction reactions (ORR) can be divided into two pathways depending on the number of electrons transferred in the reaction. The first is the $4e^-$ ORR, in which O_2 is directly reduced in one step to generate H_2O, which provides important theoretical and experimental support for fuel cell technology (Norskov et al., 2004; Anderson and Albu, 1999; Anderson and Albu, 1999; Panchenko et al., 2004; Keith and Jacob, 2010; Tripkovi et al., 2010; Sha et al., 2011; Jinnouchi et al., 2011; Viswanathan et al., 2012; Fantauzzi et al., 2015). However, due to the slow reduction rate of oxygen at the cathode, this problem seriously hinders the development of fuel cells, which makes the research of efficient ORR electrocatalyst extremely urgent (Katsounaros et al., 2013; Jung et al., 2012; Zhang et al., 2012; Chang et al., 2013; Ma et al., 2013; Feng and Frei, 2009; Liang et al., 2012; Gong et al., 2013; Zhou and Sunarso, 2013; Deng et al., 2013; Li et al., 1805; Jian et al., 2014; Li et al., 2014; Liang et al., 2011; Suntivich et al., 2011; Jin et al., 2013). The precious metal Pt/C is the best $4e^-$ ORR catalyst known at present, but the commercial application of Pt/C catalyst is severely limited due to the scarce reserves of Pt metal on Earth and the complex production and purification process (Hubert et al., 2009; Guo et al., 2013; Cui et al., 2020; Ding et al., 2019; Feng et al., 2020; Hu et al., 2018). Therefore, scholars are devoted to developing a cheap and efficient cathode $4e^-$ ORR electrocatalyst that can replace Pt/C catalyst.

The second reduction route is to dissolve oxygen at a suitable cathode interface and generate hydrogen peroxide through $2e^-$ ORR process. The strong oxidation of hydroxyl radicals decomposed by H_2O_2 will oxidize all organic pollutants in sewage without selectivity, until all toxic and harmful substances in water are oxidized to CO_2 and H_2O. At present, China's water pollution is extremely serious, and the water organic pollutants involved in papermaking, pesticide, leather, pharmaceutical, dye, pesticide and other industries, its sewage discharge complex composition, toxicity greater, concentration higher, difficult to degrade, these pollutants have great harm to human, Such as stunting infant growth, metabolic disorders, increased cancer rates, and damage to the human immune system (Jose et al., 2006; Siahrostami et al., 2014; Ichiro et al., 2003; Martínez-Huitle and Ferro, 2006). Electrochemical oxidation technology has largely solved the problem of the treatment of refractory organic pollutants in sewage, so as to improve the utilization efficiency of water and reduce the harm of organic pollutants to human health. At present, the $2e^-$ ORR catalysts with the best performance are made of Au, Ag, Hg and other precious metals and noble metal alloys.

Peer review under responsibility of King Saud University.
* Corresponding authors.
E-mail addresses: jjc1983@126.com (J. Jia), jml@imnu.edu.cn (M. Jia).

https://doi.org/10.1016/j.arabjc.2024.105624
Received 18 June 2023; Accepted 9 January 2024
Available online 11 January 2024

The yield of H_2O_2 of these noble metals can reach more than 95 %. But also because of its high price, scarce reserves and other problems cannot be large-scale production (Lu and Wei, 2012; Mei et al., 2014; Knupp et al., 2010). Therefore, researchers are working to develop cheap and efficient cathodic ORR electrocatalysts to replace precious metals and their alloys.

The ORR catalyst mainly changes the electronic structure and microscopic geometric configuration of its surface, so that oxygen molecules are adsorbed on the electrode surface in a suitable way, causing it to change the ORR path (Jiang et al., 2018). At present, rare earth metals are especially abundant in Inner Mongolia, and have excellent performance as electrode materials for ORR. Rare earth elements have extremely special electron structure: $[Xe]4f^m5d^n6s^2$, and abundant d-orbital electrons. The successful incorporation of rare earth metals improves the oxygen storage capacity and lattice oxygen activity of the catalyst, improves the catalytic activity of the interface of active metal particles, improves the dispersion of active metals, and reduces the amount of precious metals (Zhan et al., 2014). La_2O_3-NCNTs hybrid prepared by Wang et al. demonstrated that La-O and C-O bonds could enhance the activity of the $4e^-$ ORR (Wang et al., 2017). Soren et al. prepared nitrogen-doped cerium oxide composite graphene, which can realize the $4e^-$ ORR (Soren et al., 2019), however, the $2e^-$ ORR hydrogen peroxide yield of CeO_2 doped catalyst is more than 70 %, and the ORR electron transfer number is about 2.7 (Soren et al., 2016). In addition, Pd-$CeO_{2\text{-NR}}$/C catalyst prepared by Perla C et al. Compared with Pd/C nanomaterials, the successful incorporation of cerium oxide will greatly enhance the catalytic activity and electrochemical stability of $4e^-$ ORR (Meléndez-González et al., 2020). CeO_2/C catalyst showed excellent $2e^-$ ORR catalytic activity under alkaline conditions, and it was found in this study that the increase of oxygen content on the surface greatly improved the selectivity of H_2O_2 (Assumpção et al., 2013). Ipsha Hota et al. (Hota et al., 2020) studied catalysts prepared by four different rare earth oxides (Pr, Nd, Sm, Gd), and found that volcanic carbon had the highest selectivity of H_2O_2 with Nd_2O_3, reaching 91.91 %. The excellent $2e^-$ ORR performance of the catalyst was attributed to the synergistic interaction between carbon and rare earth oxides.

These studies indicate that rare earth oxides play an important role in the ORR reaction path. It has certain research value to explore the role of rare earth in ORR process. In this paper, the characteristic resource milk of Inner Mongolia is used as biomass carbon material, and the mixture of waste milk and salt in the production pipeline is simulated to recycle and reuse, so as to reduce the cost of the preparation method. The lanthanide contraction of rare earth elements and the fact that the f orbitals are not completely occupied by electrons lead to their unique chemical properties. Milk was used as a biomass-based carbon material and different rare earth metals $La(NO_3)_3{\cdot}6H_2O$ was doped in the catalyst using a salt template method to prepare three-dimensional porous biomass carbon based catalysts for ORR applications. The rare earth metal compounds were doped with NaCl as the template agent, and oxide crystals were formed in nanopores by roasting. After removing the hard template, the corresponding mesoporous materials can be prepared and electrocatalyzed. The catalyst was used as an electrode material for $2e^-$ORR, and the conditions such as milk to NaCl ratio and carbonization temperature during the preparation process were optimized using rotating disc electrode (RDE) and rotating ring disc electrode (RRDE), and the effects of surface oxygen content and miscellaneous elements such as nitrogen and phosphorus content on the ORR pathway were investigated in conjunction with the physical characterization.

2. Experimental section

2.1. Chemical reagents

$La(NO_3)_3{\cdot}6H_2O$, $Nd(NO_3)_3{\cdot}6H_2O$, $Pr(NO_3)_3{\cdot}6H_2O$, $Gd(NO_3)_3{\cdot}6H_2O$, $Sm(NO_3)_3{\cdot}6H_2O$, and NaCl is purchased from Sinopharm Chemical Reagent Co., Ltd. Milk purchased from Inner Mongolia Shenniu Co., Ltd. All reagents are pure and no other manipulations are performed.

2.2. Synthesis of materials

11 g of milk and 10 g of NaCl were mixed, and $La(NO_3)_3{\cdot}6H_2O$ was added to dissolve, and the dissolved liquid was completely frozen using liquid nitrogen to obtain the powder. The treated powder was calcined in a tube furnace at 800 °C for 2 h with a heating rate of 5 °C/min, and the whole process was completed under the protection of argon gas. The samples were centrifuged and filtered several times with ultrapure water, and then dried in a vacuum oven at 80 °C. After drying, the samples were again transferred to a tube furnace and calcined at 1000 °C for 2 h with a heating rate of 5 °C/min, and the whole process was also completed under argon protection.

2.3. Physical characterization

The morphology of the catalyst was characterized by scanning electron microscopy (SEM). The particle sizes of the catalysts were further characterized by transmission electron microscopy (TEM). The catalysts and crystal structures were analyzed by X-ray diffraction (XRD). The surface elements of the catalysts as well as the chemical states were analyzed by x-ray photoelectron spectroscopy (XPS).

2.4. Electrochemical characterization

The required slurry for the test was prepared by fully dispersing 2 mg of catalyst in 400 μL of prepared Nafion solution and sonicated in a sonicator for 0.5 h. The ultrasonic dispersed slurry was evenly coated on the electrode twice and dried. The ORR electrochemical tests of the catalysts were all measured in saturated KOH solution (0.1 M) using a rotating disk electrode.

The dye degradation performance test can be performed to determine the concentration of rhodamine B standard solution by measuring the absorbance of the solution after a certain reaction time to calculate the degradation rate of rhodamine B. A simple dye degradation device was assembled by adding LaOCl-NPC as the working electrode, Hg/HgO as the reference electrode and carbon rod as the counter electrode on a drop of carbon paper with an additional potential of 0.6 V. A certain amount of rhodamine B was added to 0.1 M KOH electrolyte.

3. Results and discussion

Using the salt template method, milk was mixed with NaCl in proportion, $La(NO_3)_3{\cdot}6H_2O$ was added to dissolve, and the dissolved liquid was freeze-dried, calcined, centrifuged, extracted, and finally the sample was ground for 0.5 h. The rare earth-doped biomass carbon-based catalyst was obtained (Scheme 1).

As can be seen from the XRD plots in Fig. 1 and Figure S1, it can be seen that the samples prepared by doping $La(NO_3)_3{\cdot}6H_2O$, $Nd(NO_3)_3{\cdot}6H_2O$, $Pr(NO_3)_3{\cdot}6H_2O$, $Gd(NO_3)_3{\cdot}6H_2O$, $Sm(NO_3)_3{\cdot}6H_2O$ correspond to the standard comparison cards PDF # 88–0064, PDF # 43–1023, PDF # 08–0046, PDF # 47–1111, PDF # 09–0385, PDF # 73–2403, PDF # 11–0414, PDF # 11–0609, indicating that the catalysts correspond to LaOCl-NPC, NdO_x-NPC, PrO_x-NPC, GdO_x-NPC, SmO_x-NPC, respectively. The average grain size of 60 nm for LaOCl-NPC can be calculated by Scherrer formula based on the relevant data obtained by XRD diffraction peaks. The XRD pattern of LaOCl series catalysts is relatively consistent with the peak of the standard comparison card, and the minor difference may be due to the difference of intermediates under different calcination temperatures, resulting in minor changes in the spectrum. With the increase of calcination temperature, defects will increase, resulting in more active sites on the catalyst surface, which is conducive to the progress of ORR.

The degree of defects of the catalysts was obtained from the Raman spectra in Fig. 2(a), where the D and G peaks were found at 1354 cm^{-1}

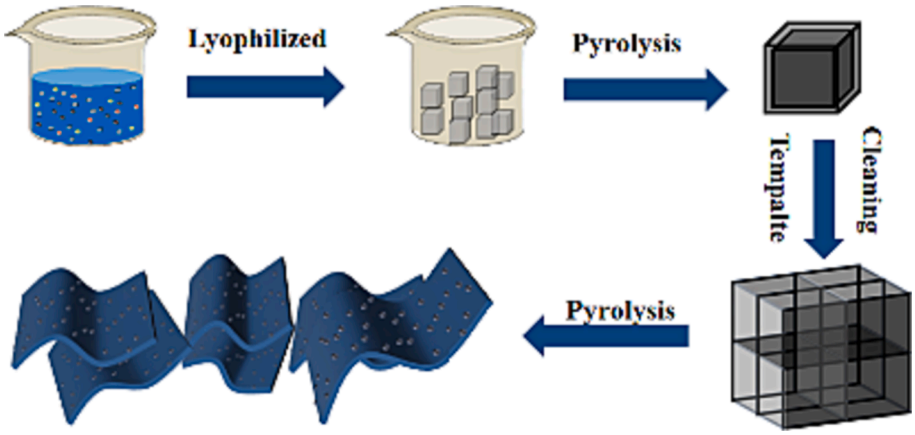

Scheme 1. Process of synthesizing LaOCl-NPC.

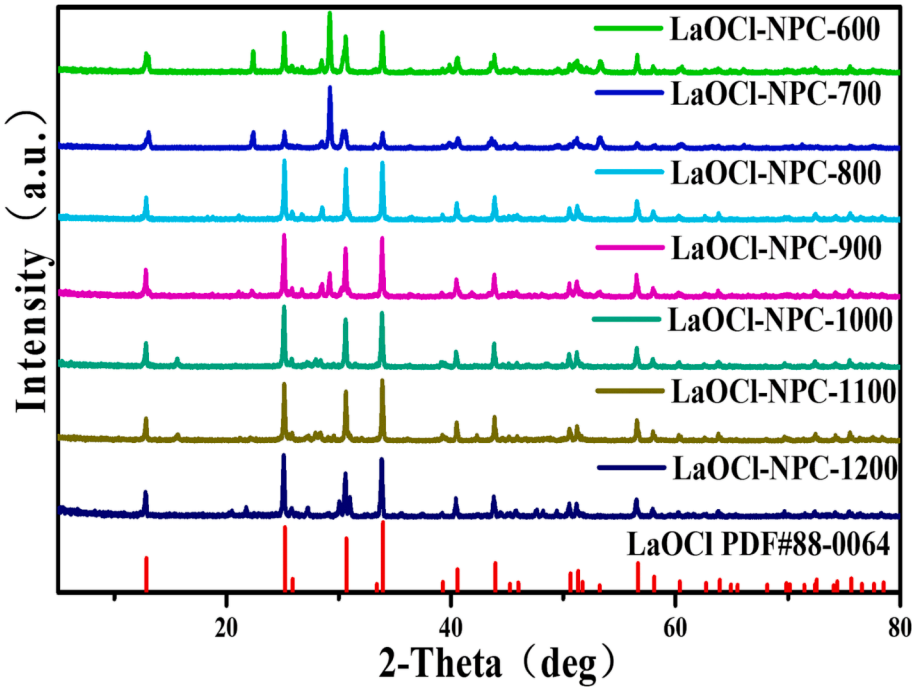

Fig. 1. XRD spectra of -LaOCl-NPC at different temperatures.

and 1587 cm^{-1}, and the I_D/I_G ratio of the prepared samples was always around 1 with increasing temperature, which proves that the degree of defects of the catalysts is increasing and the electron transport is faster, leading to better activity and stability. The fine spectra of C 1 s from Fig. 2(b) are obtained at binding energies of 287.9 eV, 284.8 eV and 283.8 eV corresponding to O-C = O bond, C = N and C–C, C = C bonds, respectively. Fig. 2(c) shows the peaks for La 3d. There are two pairs of peaks corresponding to La3d 3/2 and La3d 5/2 respectively. From Fig. 2 (d), the O 1 s peaks can be divided into three main peaks with binding energies of 529.6 eV, 531.4 eV and 533.3 eV mainly attributed to the formation of lattice oxygen, –COOH and –OH on the catalyst surface.

Fig. 2(e) shows the N 1 s fine spectrum of the catalyst LaOCl-NPC. From the figure, it can be seen that LaOCl-NPC-700 and LaOCl-NPC-900 correspond to pyridine nitrogen, pyrrole nitrogen, and oxidized nitrogen at binding energies of 397.4 eV, 400.1 eV, and 405.8 eV. The total peak area of N 1s of this series of catalysts was gradually decreasing at increasing temperature, even the disappearance of LaOCl-NPC-1100 pyridine nitrogen oxidized nitrogen were also completely disappeared. This implies that the total N content of the LaOCl-NPC catalyst gradually decreases during the temperature increase, which is attributed to the volatilization of N with the small molecules formed during the high temperature process at elevated temperatures. From Fig. 2(f), the binding energy of P 2p at 133.6 eV corresponds to the P-O bond, and the content of P is continuously decreasing when the temperature increases, but the relative content of P element increases and the peak area increases due to the large loss of N element in LaOCl-NPC-1100. The elemental contents of the LaOCl-NPC catalysts after calcination at each temperature are listed in Table S1. it is obvious from Table S1 that the changes in the contents of N and P are consistent with the results obtained from the XPS spectra.

The surface morphology of the catalyst LaOCl-NPC was observed using SEM. As shown in Fig. 3 (a) and (b), the catalyst LaOCl-NPC shows a thin layered three-dimensional structure, and such catalysts have a larger specific surface area. From BET, it can be seen that LaOCl-NPC-1200 has a larger specific surface area of 429.7 m^2/g (Table S2), which can expose more active sites and thus increase the ORR performance. The thin layered structure of the catalyst LaOCl-NPC was further confirmed by TEM images (Fig. 3(c) and (d)), where LaOCl compounded

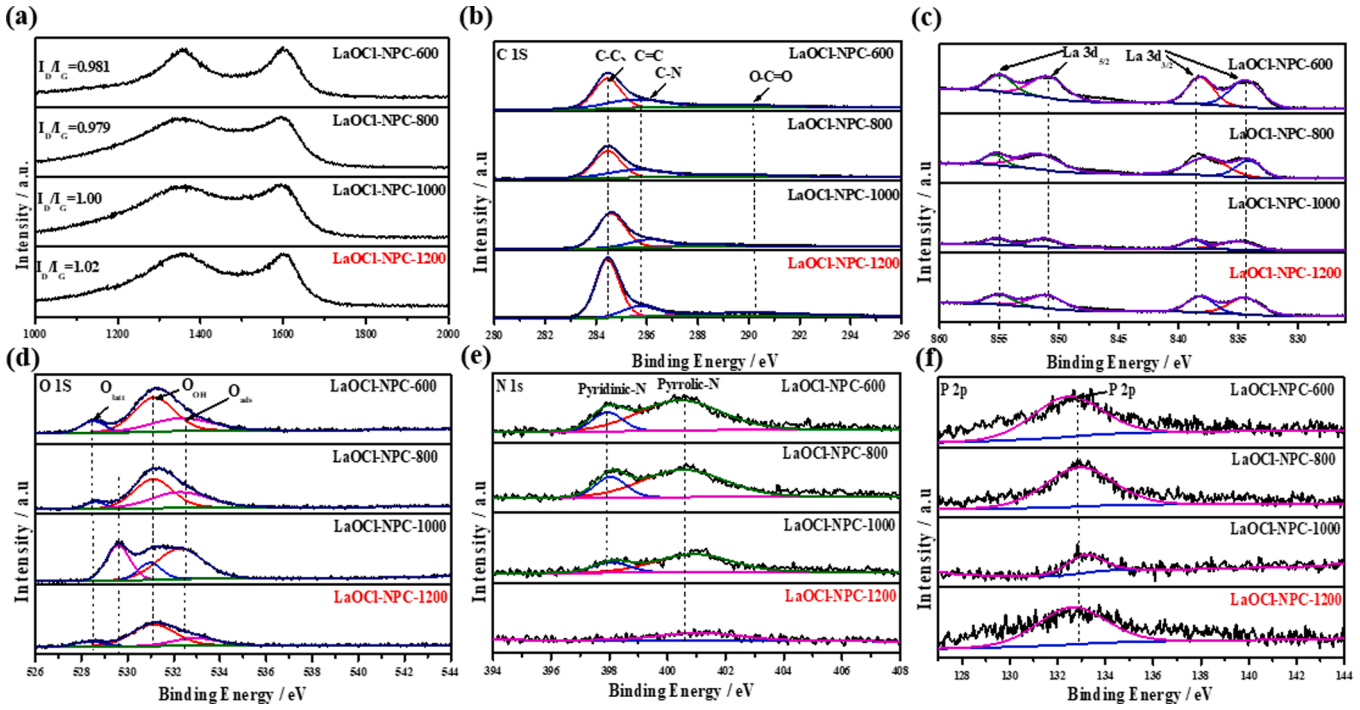

Fig. 2. (a) Raman Spectrum for catalyst LaOCl-NPC; XPS high resolution of LaOCl-NPC for (b) C 1 s, (c) La 3d, (d) O 1 s, (e) N 1 s, (f) P 2p region.

on the surface of the thin layered structure could synergize with carbon to promote the ORR and increase the activity of the reaction. The characterization by HR-TEM (Fig. 3(e)) can be obtained that the stripes with a lattice spacing of 0.29 nm correspond to the catalyst LaOCl-NPC (1 1 0) crystal plane. (Xiaolei et al., 2018) Fig. 3(f) shows the physical phase analysis of the polycrystalline diffraction ring, from which it can be clearly observed that the catalyst LaOCl-NPC has a polycrystalline shape, which proves the polycrystalline structure of the catalyst LaOCl-NPC. Finally, the EDS elemental mapping plot as shown in Fig. 3(g) further indicates that the four elements C, N, P, Cl, O and La are uniformly distributed in the catalyst LaOCl- NPC.

A three-electrode system was used for cyclic voltammetric testing of the catalyst, with the RDE electrode as the working electrode, the reference electrode as Hg/HgO, and the carbon rod selected as the counter electrode. Figure S2 shows the test results in 0.1 mol-L^{-1} KOH electrolyte, where the red and black curves are the CV curves for oxygen-saturated argon saturated conditions, respectively. It can be observed that no oxygen reduction peaks are found under argon saturated conditions. On the contrary, the reduction peak of oxygen can be clearly seen under oxygen saturated conditions, which can prove the ORR performance of all the series catalysts.

Figure S3 show the LSV plots of the LaOCl-NPC catalyst at different rotational speeds, and again as the rotational rate of the RDE increases, the diffusion rate of the oxygen molecules also increases, ultimately leading to an increase in the limiting diffusion current density. To investigate the ORR electron transfer pathway of catalyst on LSV test data, the Koutecky-Levich (K-L) equation was used to calculate the electron transfer number and to plot the K-L curve.

As shown in Figure S4, by optimizing the calcination temperature, we likewise conducted the comparison samples LaOCl-NPC-600, LaOCl-NPC-700, LaOCl-NPC-800, LaOCl-NPC-900, LaOCl-NPC-1000, LaOCl-NPC-1100, LaOCl-NPC-1200, The slope of the K-L curve was calculated and the electron transfer numbers of the ORR of the catalysts LaOCl-NPC-600, LaOCl-NPC-700, LaOCl-NPC-800, LaOCl-NPC-900 were obtained as 2.6, 2.8, 3.1, 3.1, respectively. When the temperature was increased to 1000 °C, the electron transfer number increased significantly to 3.3. However, the electron transfer numbers were 3.2, 3.0, for catalysts LaOCl-NPC-1100, LaOCl -NPC-1200, respectively, after the temperature continued to increase. From the calculations, it is obtained that the electron transfer number of ORR is a $2e^-$ to $4e^-$ process with increasing temperature, which is attributed to the deepening of graphitization of carbon during this process, leading to the enhancement of electrical conductivity. Meanwhile, the synergistic effect of N with LaOCl-NPC and the addition of heteroatoms such as N and P can cause carbon defects to produce active sites, which eventually leads to the ORR process of the catalyst LaOCl-NPC-1000 belongs to the $4e^-$process. As the calcination temperature continues to increase, the N and P elements continue to spill out with the small molecules leading to a decrease in the synergistic effect, so the ORR process of the catalyst starts to change to a $2e^-$process. Since the K-L equation used is an empirical equation and the parameters are somewhat different from the ideal values, further testing and analysis of this series of catalysts was carried out using RRDE in order to confirm the changes in the reaction pathway of the process ORR.

To determine the variation of the oxygen reduction pathway for this series of catalysts, the same test conditions were used with RRDE as the working electrode and also in an oxygen-saturated 0.1 M KOH electrolyte to obtain LaOCl-NPC-600, LaOCl-NPC-700, LaOCl-NPC-800, LaOCl-NPC-900, LaOCl-NPC-1000, LaOCl-NPC-1100, LaOCl-NPC-1200 at 1600 rpm for the selectivity of LSV curves H_2O_2 and the electron transfer number.

From the calculated results Fig. 4 (c) and (d), it can be seen that there is a certain regular variation of the H_2O_2 yield and the number of transferred electrons of the catalyst at a potential of 0.6 V. Starting from LaOCl-NPC-600, the hydrogen peroxide yield of the catalyst decreases continuously from 26 % to 7 % for LaOCl-NPC-1000, and the number of transferred electrons increases from 2.6 to 3.3, indicates that the ORR process of the catalyst is biased from a $2e^-$process to a $4e^-$process at an initial increase in temperature. This is due to the poor electrical conductivity of carbon at low temperatures and the subsequent increase in the electrical conductivity of carbon at increasing temperatures. And the XPS results proved that the content of N and P was more at low temperature, and the content of O was increasing and the peak area of LaOCl was also increasing during the process, which means more LaOCl was produced. The temporal Raman results show that the ratio of the D-peak to the G-peak is increasing after increasing the temperature, indicating a

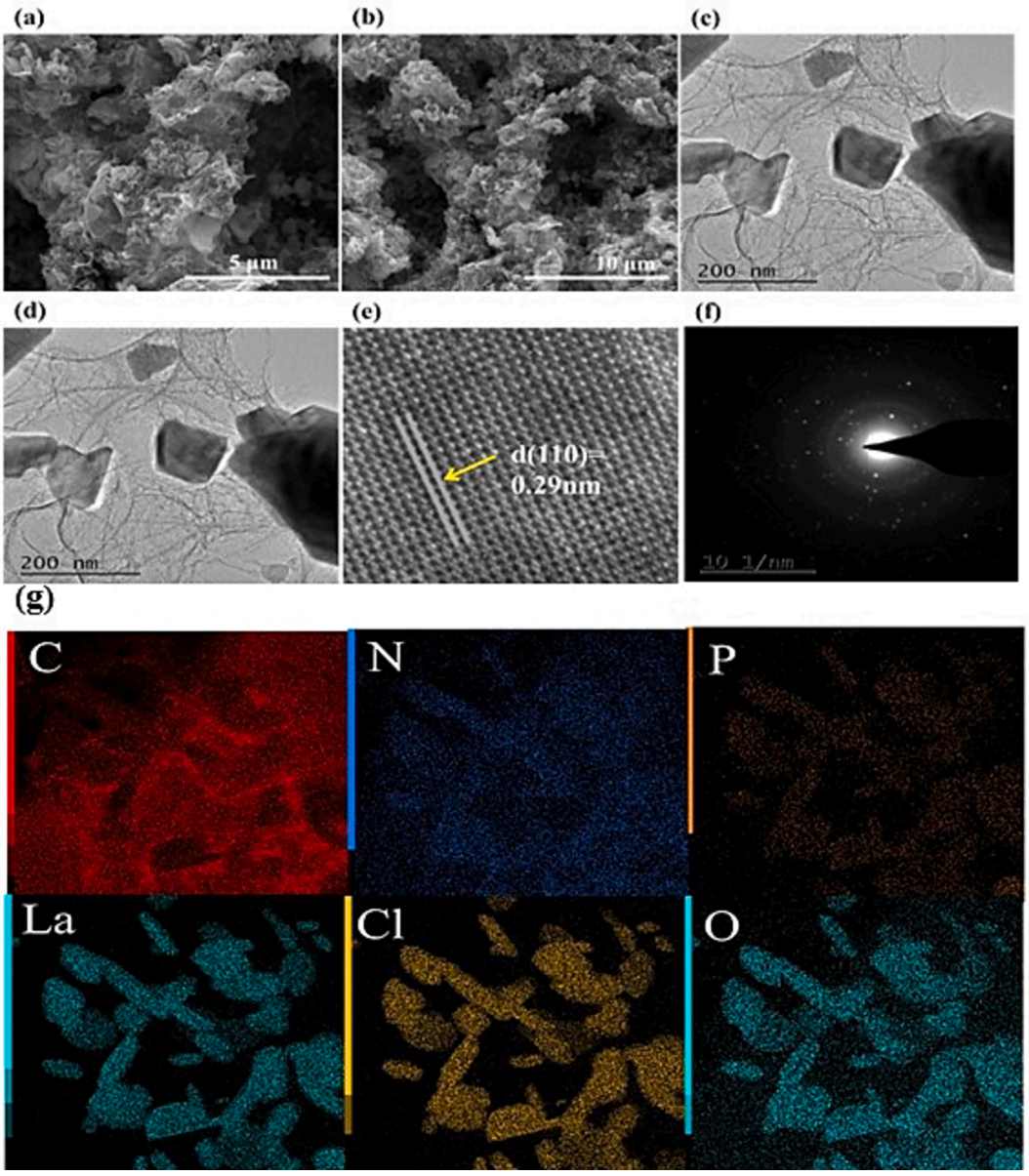

Fig. 3. (a), (b) SEM images of LaOCl-NPC, (c), (d) TEM images of LaOCl-NPC, (e), (f) HR-TEM images of LaOCl-NPC, (g) EDS mapping of LaOCl-NPC.

significant increase in defects. It is shown that the synergistic effect of N and LaOCl in carbon materials, carbon defects and heteroatoms can modulate the electronic structure and surface polarity of carbon are favorable to increase the catalytic active site of 4e$^-$ORR, and the generation of LaOCl and the increase of defects also play a crucial role in ORR catalysis. When the catalyst calcination temperature is increased to 1200 °C, it can be seen from Fig. 4 (c) and (d) that the hydrogen peroxide yield continues to increase and the electron transfer number is increasing as well as the increase of defects also plays a crucial role in ORR catalysis. At this point, the catalyst calcination temperature was increased to 1200 °C from 4e$^-$ to 2e$^-$. This is because as the temperature continues to increase, the synergistic effect of LaOCl and N elements decreases and the amount of LaOCl is increasing due to the continuous overflow of doped N and P elements and the disappearance of pyridine nitrogen during high temperature calcination in the process. The increase in oxygen content led to an increase in the activity and selectivity of the ORR, resulting in the dominance of the 2e$^-$pathway and the highest peroxide selectivity of 70 % as well as the number of transferred electrons of 2.7 at LaOCl-NPC-1200. When the temperature was increased again, the decrease of O content and the slight decrease of LaOCl peak area implied that the amount of LaOCl was decreasing, which led to the tendency of decreasing H_2O_2 selectivity again. This phenomenon once again proved that the catalyst LaOCl-NPC surface oxygen element content had a great promotion effect on ORR. The catalyst was finally determined to have the highest H_2O_2 selectivity at a milk to NaCl ratio of 1:10 and a calcination temperature of 1200 °C, which is a more ideal 2e$^-$ ORR catalyst. The electron transfer number and H_2O_2 yield were obtained by RRDE test. In terms of reaction mechanism, the charge transfer impedance of the catalyst is relatively large, which weakens the ability of OOH* free radical to combine with the enriched electrons on the catalyst surface, and causes the reaction to generate H_2O_2 in the direction of two electrons. (Zhipeng et al., 2020)

$$H_2O_2(\%) = 200^*(I_r/N)/(I_d + I_r/N) \quad (1)$$

$$N = 4^*(I_d/(I_d + I_r/N) \quad (2)$$

Where I_d: rotating disc current, I_r: rotating ring disc current, and N: collection efficiency of the platinum ring on the rotating ring disc electrode.

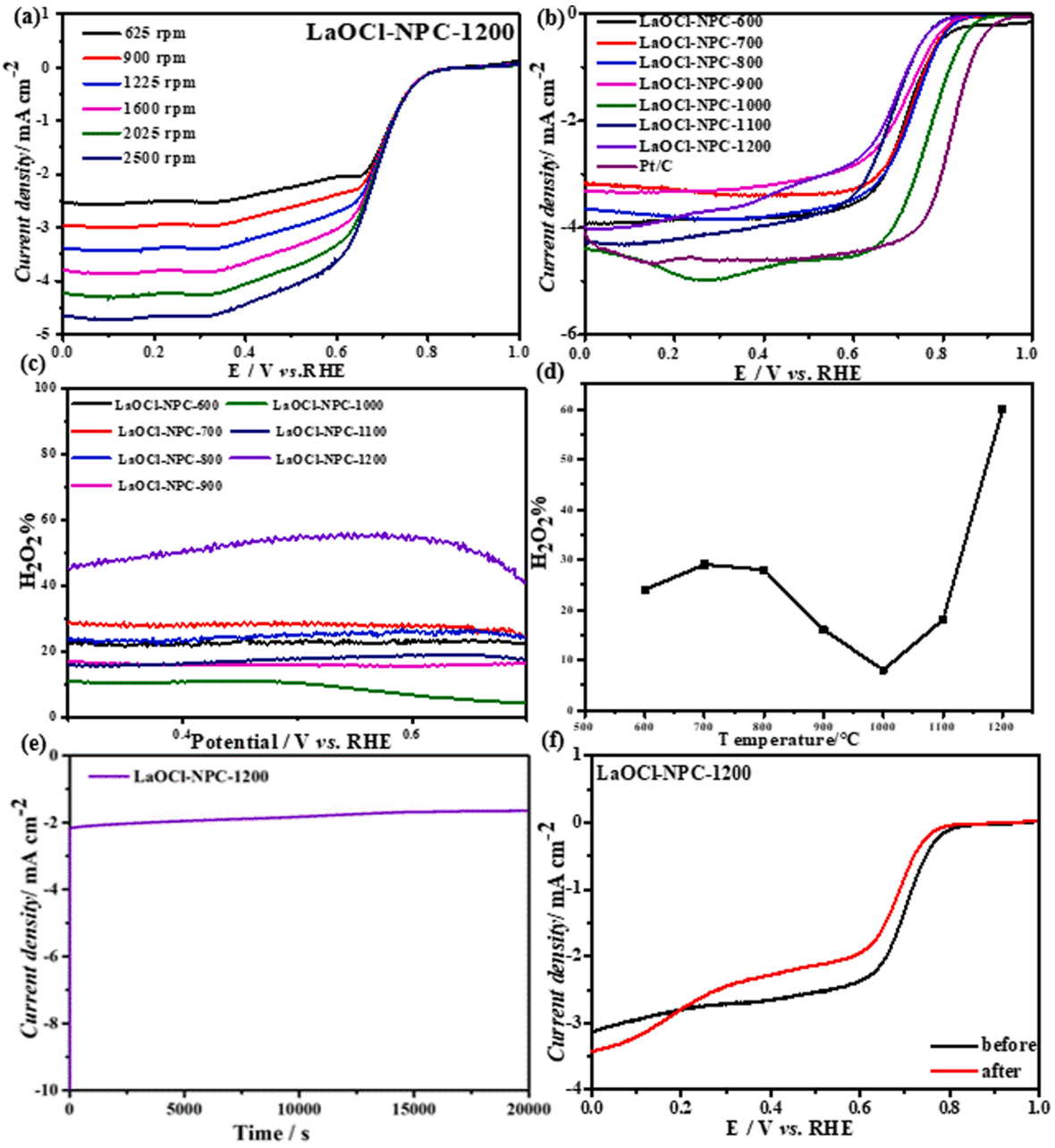

Fig. 4. (a) LSV curve of LaOCl-NPC-1200, (b) LSV curves for LaOCl-NPC and commercial Pt/C, (c), (d)shows the hydrogen peroxide yields of catalyst LaOCl- NPC at different temperatures, (e)i-t curve (f) LSV curves before and after i-t test of LaOCl-NPC-1200.

Stability and durability are also important indicators for catalyst evaluation. Fig. 4(e-f) shows the i-t test for up to 20,000 s in an O_2-saturated 0.1 M KOH solution, and the results show that the current density is well maintained. The LSV diagram of the catalyst before and after 20,000 s of testing shows that the negative shift of peak potential and half-wave potential is relatively small. Therefore, LaOCl-NPC has good stability.

Finally, Figure S5 shows the hydrogen peroxide yields of the three catalysts Nd-NPC, Pr-NPC and La-NPC, which also generate chlorine oxides, were compared, and it was found that the hydrogen peroxide yield of catalyst La-NPC was at 70 % at 0.6 V, while the H_2O_2 yield of catalyst Pr-NPC was 65 %, and the H_2O_2 yield of catalyst Nd-NPC was only 50 %. In most of the other representative literatures, the H_2O_2 yield exceeds 80 %, (Zhaoquan et al., 2021; Norah et al., 2022; Hongyuan et al., 2020) while in this paper, the H_2O_2 yield is nearly 70 %. Importantly, the catalyst has a higher initial potential of 0.82 V in ORR, and its stability is also good. The reason for this phenomenon is that due to the unique electronic structure of rare earth elements, Nd and Pr generate new 4f orbitals, resulting in lower energy, which leads to a decrease in the formation energy of oxygen vacancies, resulting in a decrease in the final H_2O_2 yield.

The excellent $2e^-$ORR performance of the catalyst LaOCl-NPC provides a theoretical basis for the construction of a simple pollutant degradation device. The catalyst LaOCl-NPC was used as the working electrode, the reference electrode was Hg/HgO, the carbon rod was selected as the counter electrode, rhodamine B was the target degradation substance, and the applied potential was 0.6 V. A simple pollutant degradation device was formed by using 0.1 M KOH as the electrolyte, to which a certain amount of rhodamine B was added and its concentration change was tested after a period of time. Figure S6(a) shows the standard curve of absorbance variation with the concentration of rhodamine B. Figure S6(b) shows the concentration variation of

rhodamine B after 8 h of testing, it can be clearly found that the concentration of rhodamine B has a significant decrease after 8 h of catalyst degradation. Although the concentration of rhodamine B decreased significantly from 8.656 mg/L to 4.850 mg/L, the degradation process took longer and rhodamine B was not completely degraded, probably because the prepared H_2O_2 decomposed faster and could not be stored in the electrolyte for a long time and the amount of catalyst used in the experiment was small, resulting in a smaller H_2O_2 concentration in the electrolyte and therefore a lower degradation efficiency of rhodamine B.

4. Summary

In this paper, LaOCl-NPC was identified as an excellent $2e^-$ ORR catalyst in alkaline solution by doping with different rare earths. The successful synthesis of the rare-earth composite biocarbon-based catalyst LaOCl-NPC was confirmed by the physical characterization of the catalyst by XRD, XPS, Raman, SEM, TEM, HR-TEM, etc. The electrochemical testing of the catalyst LaOCl-NPC was combined with the physical characterization to obtain that the LaOCl-NPC catalyst has a good $2e^-$ ORR performance. The hydrogen peroxide yield reached about 70 %, which is a more ideal $2e^-$ ORR catalyst. Since La has no electrons in the 4f orbital, it is easier to generate oxygen vacancies compared with other rare earth metals, which enhances its $2e^-$ ORR performance.

Declaration of competing interest

The authors declare that they have no known competing financial interests or personal relationships that could have appeared to influence the work reported in this paper.

Acknowledgments

We acknowledge the National Natural Science Foundation of China (Project No. 22062019), the Fundamental Research Funds for the Inner Mongolia Normal University (2022JBBJ011), Science and Technology Program of Inner Mongolia Autonomous Region, China (2020PT0003), the Key Research Program of Science and Technology at Universities of Inner Mongolia Autonomous Region (NJZZ22588), Inner Mongolia Normal University Graduate Research Innovation Fund Project (CXJJS22115) for funding this study.

Appendix A. Supplementary material

Supplementary data to this article can be found online at https://doi.org/10.1016/j.arabjc.2024.105624.

References

Anderson, A.B., Albu, T.V., 1999. Ab initio approach to calculating activation energies as functions of electrode potential: Trial application to four-electron reduction of oxygen [J]. Electrochem. Commun. 1 (6), 203–206.
Anderson, A.B., Albu, T.V., 1999. Ab initio determination of reversible potentials and activation energies for outer-sphere oxygen reduction to water and the reverse oxidation reaction [J]. J. Phys. Chem. Lett. 121 (50), 11855–11863.
Assumpção, M., Moraes, A., Souza, R.D., et al., 2013. Influence of the preparation method and the support on H2O2 electrogeneration using cerium oxide nanoparticles [J]. Electrochim. Acta 111, 339–343.
Chang, S.P., Kim, J.H., Yong, J.P., 2013. Catalytic activity of carbon-sphere/Co3O4/RuO2 nanocomposite for Li-air batteries [J]. J. Electroceram. 31, 224–230.
Cui, L., Chen, M., Huo, G., et al., 2020. FeCo nanoparticles wrapped in N-doped carbon derived from Prussian blue analogue and dicyandiamide as efficient oxygen reduction electrocatalysts for Al-air batteries [J]. Chem. Eng. J. 395, 125158.
Deng, D., Yu, L., Chen, X., et al., 2013. Iron encapsulated within pod-like carbon nanotubes for oxygen reduction reaction [J]. Angew. Chem. Int. Ed. 125 (1), 389–393.
Ding, J.T., Ji, S., Wang, H., et al., 2019. Mesoporous cobalt selenide/nitrogen-doped carbon hybrid as bifunctional electrocatalyst for hydrogen evolution and oxygen reduction reactions [J]. J. Power Sources 423 (31), 1–8.
Fantauzzi, D., Zhu, T., Mueller, J.E., et al., 2015. Microkinetic modeling of the oxygen reduction reaction at the Pt (111)/gas interface [J]. Catal. Lett. 145 (1), 451–457.
Feng, X.G., Bo, X.J., Guo, L.P., 2020. An advanced hollow bimetallic carbide/nitrogen-doped carbon nanotube for efficient catalysis of oxygen reduction and hydrogen evolution and oxygen evolution reaction [J]. J. Colloid Interface Sci. 575 (1), 69–77.
Feng, J., Frei, H., 2009. Nanostructured cobalt oxide clusters in mesoporous silica as efficient oxygen-evolving catalysts [J]. Angew. Chem. Int. Ed. 121 (10), 1873–1876.
Gong, M., Li, Y., Wang, H., et al., 2013. An advanced Ni-Fe layered double hydroxide electrocatalyst for water oxidation [J]. J. Am. Chem. Soc. 135 (23), 8452–8455.
Guo, S., Zhang, S., Sun, S., 2013. Tuning nanoparticle catalysis for the oxygen reduction reaction [J]. Angew. Chem. Int. Ed. 52 (33), 8526–8544.
Hongyuan, S., Aurora, N., Dominic, R., et al., 2020. Stable and selective electrosynthesis of hydrogen peroxide and the electro-Fenton process on CoSe2 polymorph catalysts [J]. Energ. Environ. Sci. 13, 4189–4203.
Hota, I., Debnath, A.K., Muthe, K.P., et al., 2020. Electrocatalytic production of hydrogen-eroxide from molecular oxygen by rare earth (Pr, Nd, Sm or Gd) oxide nanorods [J]. Electroanalysis 32 (11), 2521–2527.
Hu, E., Yu, X.Y., Chen, F., et al., 2018. Graphene layers-wrapped Fe/Fe5C2 nanoparticles supported on N-doped graphene nanosheets for highly efficient oxygen reduction [J]. Adv. Energy Mater. 8 (9), 1702476.
Hubert, A., Gasteiger, N.M., et al., 2009. Chemistry. Just a dream-or future reality ? [J]. Science 324 (5923), 48–49.
Ichiro, Yamanaka, Takeshi, et al. Direct and continuous production of hydrogen peroxide with 93% selectivity using a fuel-cell system [J]. Angewandte Chemie International Edition, 2003, 42 (31): 3653-3655.
Jian, Z., Liu, P., Li, F., et al., 2014. Core-shell-structured CNT@RuO2 composite as a high-performance cathode catalyst for rechargeable Li-O2 batteries [J]. Angew. Chem. Int. Ed. 53 (2), 442–446.
Jiang, Y.Y., Ni, P.J., Chen, C.X., et al., 2018. Selective electrochemical H2O2 production through two-electron oxygen electrochemistry [J]. Adv. Energy Mater. 8 (31), 1801909.
Jin, Won, Kim, et al. Self-organized one-dimensional cobalt compound nanostructures from CoC_2O_4 for superior oxygen evolution reaction [J]. The Journal of Physical Chemistry C, 2013, 117 (45): 23712-23715.
Jinnouchi, R., Kodama, K., Hatanaka, T., et al., 2011. First principles based mean field model for oxygen reduction reaction [J]. PCCP 13, 21070–21083.
Jose, M, Campos-Martin, et al. Hydrogen peroxide synthesis: an outlook beyond the anthraquinone process [J]. Angewandte Chemie International Edition, 2006, 45 (42): 6962-6984.
Jung, K., Lee, J., Yoon, S., et al., 2012. Manganese oxide/carbon composite nanofibers: electrospinning preparation and application as a bi-functional cathode for rechargeable lithium–oxygen batteries [J]. J. Mater. Chem. 22, 21845.
Katsounaros, I., Cherevko, S., Zeradjanin, A.R., et al., 2013. Oxygen electrochemistry as a cornerstone for sustainable energy conversion [J]. Angew. Chem. Int. Ed. 53 (1), 102–121.
Keith, J.A., Jacob, T., 2010. Theoretical studies of potential-dependent and competing mechanisms of the electrocatalytic oxygen reduction reaction on Pt (111) [J]. Angew. Chem. Int. Ed. 49 (49), 9521–9525.
Knupp, S.L., Vukmirovic, M.B., Haldar, P., et al., 2010. Platinum monolayer electrocatalysts for O2 reduction: Pt monolayer on carbon-supported PdIr nanoparticles [J]. Electrocatalysis 1, 213–223.
Li, F., Chen, Y., Tang, D.M., et al., 2014. Performance-improved Li–O2 battery with Ru nanoparticles supported on binder-free multi-walled carbon nanotube paper as cathode [J]. Energ. Environ. Sci. 7 (5), 1648–1652.
Li, Y.G., Gong, M., Liang, Y.Y., et al., 1805. Advanced zinc-air batteries based on high-performance hybrid electrocatalysts [J]. Nat. Commun. 2013, 4.
Liang, Y., Li, Y., Wang, H., et al., 2011. Co3O4 nanocrystals on graphene as a synergistic catalyst for oxygen reduction reaction [J]. Nat. Mater. 10 (10), 780–786.
Liang, Y., Wang, H., Zhou, J., et al., 2012. Covalent hybrid of spinel manganese-cobalt oxide and graphene as advanced oxygen reduction electrocatalysts [J]. J. Am. Chem. Soc. 134 (7), 3517–3523.
Lu, Y., Wei, C., 2012. Size effect of silver nanoclusters on their catalytic activity for oxygen electro-reduction [J]. J. Power Sources 197 (1), 107–110.
Ma, S., Sun, L., Cong, L., et al., 2013. Multiporous MnCo2O4 microspheres as an efficient bifunctional catalyst for nonaqueous Li–O2 batteries [J]. J. Phys. Chem. C 117 (49), 25890–25897.
Martínez-Huitle, C.A., Ferro, S., 2006. Electrochemical oxidation of organic pollutants for the wastewater treatment: Direct and indirect processes [J]. Chem. Soc. Rev. 35 (12), 1324–1340.
Mei, D., He, Z.D., Zheng, Y.L., et al., 2014. Mechanistic and kinetic implications on the ORR on a Au(100) electrode: pH, temperature and H-D kinetic isotope effects [J]. Phys. Chem. Chem. Phys. 16 (27), 13762–13773.
Meléndez-González, P.C., Sánchez-Castro, E., Alonso-Lemus, I.L., et al., 2020. Bifunctional Pd-CeO2 nanorods/C nanocatalyst with high electrochemical stability and catalytic activity for the ORR and EOR in alkaline media [J]. ChemistrySelect 5 (44), 14032–14040.
Norah, M.B., Parbhakarn, A., Abdullah, M., et al., 2022. Enhanced electrochemical hydrogen peroxide production from surface state modified mesoporous tin oxide catalysts [J]. Int J Energy Res. 46, 9150–9165.
Norskov, J.K., Rossmeisl, J., Logadottir, A., et al., 2004. Origin of the overpotential for oxygen reduction at a fuel-cell cathode [J]. J. Phys. Chem. B 108 (46), 17886–17892.
A. Panchenko M. Koper T.E. Shubina et al. Ab Initio calculations of intermediates of oxygen reduction on low-index platinum surfaces [J] Journal of The Electrochemical Society 151 12 2004 A2016 A27.
Sha, Y., Ted, H., Merinov, B.V., et al., 2011. Oxygen hydration mechanism for the oxygen reduction reaction at Pt and Pd fuel cell Catalysts [J]. J. Phys. Chem. Lett. 2 (6), 572–576.

Siahrostami, S., Ver Da Guer-Casadevall, A., Karamad, M., et al., 2014. Enabling direct H2O2 production through rational electrocatalyst design [J]. Nat. Mater. 13 (1), 97.
Soren, S., Mohaptra, B.D., Mishra, S., et al., 2016. Nano ceria supported nitrogen doped graphene as a highly stable and methanol tolerant electrocatalyst for oxygen reduction [J]. RSC Adv. 6 (80), 77100–77104.
Soren, S., Hota, I., Debnath, A.K., et al., 2019. Oxygen reduction reaction activity of microwave mediated solvothermal synthesized CeO2/g-C3N4 nanocomposite [J]. Front. Chem. 7, 403.
Suntivich, J., Gasteiger, H.A., Yabuuchi, N., et al., 2011. Design principles for oxygen-reduction activity on perovskite oxide catalysts for fuel cells and metal–air batteries [J]. Nat. Chem. 3 (7), 546–550.
Tripkovi, V., Skúlason, E., Siahrostami, S., et al., 2010. The oxygen reduction reaction mechanism on Pt (111) from density functional theory calculations [J]. Electrochim. Acta 55 (27), 7975–7981.
Viswanathan, V., Hansen, H.A., Rossmeisl, J., et al., 2012. Universality in oxygen reduction electrocatalysis on metal surfaces [J]. ACS Catal. 2 (8), 1654–1660.
Wang Z, Feng Z, Chao J, et al. La_2O_3-NCNTs hybrids in-situ derived from $LaNi_{0.9}Fe_{0.1}O_3$-C composites as novel robust bifunctional oxygen electrocatalysts [J]. Carbon, 2017, 115: 261-270.
Xiaolei, W., Xiukun, B., Xinao, Z., et al., 2018. Excellent microwave absorption of lamellar LaOCl/C nanocomposites with LaOCl nanoparticles embedded in carbon matrix [J]. J. Alloy. Compd. 764, 701–708.
Zhan, W., Guo, Y., Gong, X., et al., 2014. Current status and perspectives of rare earth catalytic materials and catalysis [J]. Chin. J. Catal. 35 (8), 1238–1250.
Zhang, K.J., Zhang, L.X., Chen, X., et al., 2012. Mesoporous cobalt molybdenum nitride: a highly active bifunctional electrocatalyst and its application in lithium–O_2 batteries. [J]. 117 (2), 858–865.
Zhaoquan, X., Liang, J., Yuanyuan, W., et al., 2021. Enhanced electrochemical H2O2 production via two-electron oxygen reduction enabled by surface-derived amorphous oxygen-deficient TiO2−x [J]. ACS Appl. Mater. Interfaces 13 (28), 33182–33187.
Zhipeng, S., Lei, S., Hao, G., et al., 2020. Electrocatalytic synthesis of hydrogen peroxide over Au/TiO2 and electrochemical trace of OOH* intermediate [J]. Chem. Asian J. 15 (24), 4280–4285.
Zhou, W., Sunarso, J., 2013. Enhancing Bi-functional electrocatalytic activity of perovskite by temperature shock: a case study of laNiO3−δ [J]. J. Phys. Chem. Lett. 135 (23), 8452–8455.